

Article

Peristaltic Propulsion of Jeffrey Nanofluid with Thermal Radiation and Chemical Reaction Effects

Munawwar Ali Abbas¹, Muhammad Mubashir Bhatti^{2,3,*}  and Mohsen Sheikholeslami⁴

¹ Department of Mathematics, University of Baltistan Skardu, Skardu 16100, Pakistan; munawar.abbas@uobs.edu.pk

² College of Mathematics and Systems Science, Shandong University of Science and Technology, Qingdao 266590, China

³ Shanghai Institute of Applied Mathematics and Mechanics, Shanghai University, Shanghai 200072, China

⁴ Department of Mechanical Engineering, Babol Noshirvani University of Technology, Babol, Iran; mohsen.sheikholeslami@nit.ac.ir

* Correspondence: muhammad09@shu.edu.cn or mmbhatti@sdust.edu.cn

Received: 17 September 2019; Accepted: 21 November 2019; Published: 27 November 2019



Abstract: In this article, we have studied non-uniform hemodynamic nanofluid flow in the presence of an external magnetic field. The fluid contains magnetized nanoparticles in the presence of thermal radiation and chemical reaction. The magnetic field plays an essential role in targeting drugs by magnetic nanoparticles (“ferrofluids”) for different kinds of diseases in a human body. The Jeffrey viscoelastic model is employed to simulate non-Newtonian characteristics. With an approximation of long wavelength and minimal Reynolds number, a mathematical formulation has been performed. Numerical and analytical simulation has been used to examine the role of all the emerging parameters. Individual cases for the Newtonian fluid, non-Newtonian, nanofluid, and base fluid, have been exhibited numerically. A magnificent graphical correlation is additionally given with recently obtained outcomes to show the validity of the present findings and methodology.

Keywords: magnetic nanoparticles; drug delivery; thermal radiation; blood flow; chemical reaction

1. Introduction

Magnetic drug targeting plays an essential and significant role nowadays in biomedical engineering. The central theme of magnetic drug targeting is a specific delivery of the chemotherapeutic agents to their associated targets i.e., tumors, with the help of the magnetic nanoparticles (“ferrofluids”) leap to the relevant agents and an extrinsic magnetic field is applied to the desired tumor. For the first magnetic drug targeting in a human body, this was connected to bio-compatible iron-core particles of sized 100 nm diameter. These small particles were systematically controlled, and an extrinsic magnetic field was used for the shallow tumor at the inoperable places. Numerous types of magnetic carrier have been presented and introduced in the literature. Gene therapy and Drugs have been connected to magnetic nanoparticles (“Ferrofluids”) [1–3], i.e., bio-compatible Nanoscale or microscopic capsules which are filled with magnetic materials and drugs [4,5], and live cells are cultivated in a media that consists of magnetic particles so that the cell absorbs the particles and then it can be handled by the magnetic fields [6]. Chemists and nanofabricators should work on a collaboration with mathematicians, engineers, and biologists to examine how carries propagate through the live tissues and how to enhance the magnetic designs and carries the therapy process to the targeted diseases. Clinicians must involve during the whole procedure to make sure that the techniques that are introduced must meet the compelling clinical requirement and will be practically beneficial for clinical settings.

Because it is of such importance, various authors discussed the behavior of the magnetic field and the nanofluid mechanism. For instance, Misra et al. [7] theoretically studied the mechanism of

blood flow through an arterial segment. He considered the blood as an external plasma layer that does not contain red cells utilizing a Casson fluid model. Akbar et al. [8] examined the slip effects on the sinusoidal motion of the peristaltic flow of nanofluids. Tripathi and Bég [9] presented a detailed study on the peristaltic motion of a nanofluid for the case of drug delivery. However, they ignored the effects of the non-Newtonian case and obtained exact solutions. Sheikholeslami and Abelman [10] used two-phase modeling for the simulation of nanofluids and heat transfer with an axial magnetic field. Akbar et al. [11] discussed the behavior of the magnetic field with heat transfer in the presence of carbon nanoparticles propagating through a permeable channel. Entropy generation on the blood flow of a nanofluid employing analytical simulation was presented by Rashidi et al. [12]. Bhatti et al. [13] investigated blood clotting in the nanofluid flow with the gyrotactic microorganism and variable magnetic field. Iftikhar et al. [14] used copper Nanofluid with water as a base fluid propagating through a magnetized inclined tube. Abdelsalam and Bhatti [15] studied a non-Newtonian nanofluid model with hall and ion slip effects spreading through a non-uniform channel. Mekheimer et al. [16] explored the behavior of blood in the presence of gold nanoparticles using a third-grade nanofluid through a catheter. They presented an application of cancer therapy. Akram et al. [17] used a Jeffrey fluid model to determine the double-diffusive process in a nanofluid with magnetic effects. Prakash et al. [18] explored the thermal radiation, magnetic, and temperature-dependent viscosity on the nanofluid flow and presented mathematical modeling for the solar magneto-biomimetic pump. Abdelsalam and Bhatti [19] presented a new mathematical modeling for AuNP blood flow with the applications of cosmetic and tumor treatment through an annulus filled with nanofluids. A few more studies on the nanofluid and magnetic field can be found from the references [20–25].

The nanofluid flow with thermal and chemical reaction has broad applications in cooling, expulsion procedures and polymer industry. The chemical reaction can be classified as either homogeneous or heterogeneous procedures. A homogeneous response is one that happens consistently through a given stage. Conversely, a heterogeneous reaction happens in a limited district or inside the limit of a phase. Thermal and chemical response execution investigations of steam methane transforming in permeable media solar-powered thermochemical reactors were examined in detail by [26,27]. However, there are not many investigations of its impact on convective unsteadiness in nanofluids. Recently, Akbarzadeh [28] and Yadav [29] examined the effect of chemical reaction on the convective instability in a horizontal layer of nanofluids utilizing the direct soundness examination. They saw that the dependability of the framework augmented with an enlargement in the substance response parameter. Furthermore, thermochemical execution of solar-based driven changing of methane in a volumetric reactor with permeable media was numerically researched by [30,31]. However, transforming and gasification of previously mentioned carbonaceous fuels typically occur at high temperatures bringing about generally high heat dissipation. A significant expense central receiver system is required for applying the heat during this sort of high-temperature endothermic process.

The present work audits progress in and our comprehension of thermal radiation and the response of chemical reaction in magnetized nanofluid flow. The present analysis is applicable for magnetic drug targeting for various treatments in a human body. The arrangement of administering stream issues for velocity profile, temperature profile, and nanoparticle concentration profile is acquired with the assistance of the perturbation technique. The impacts of various parameters of intrigue are talked about and exhibited graphically. Our hope is that the present analysis will be beneficial for the researchers to analyze magnetic drug targeting for clinical purposes.

2. Mathematical Formulation

The two-dimensional non-uniform channel is considered with a sinusoidal wave spreading towards its dividers. The proposed geometrical structure contains blood in the presence of magnetized nanoparticles. The blood chemically reacts in the presence of thermal radiation effects. The Cartesian coordinate framework (\tilde{x}, \tilde{y}) is chose. Here, \tilde{x} -axis is considered along the centerline toward wave proliferation and \tilde{y} -axis is transverse to it (see Figure 1). B_0 is the extrinsic magnetic field quality, which

is acting along the \tilde{y} -axis and an induced magnetic field is neglected. The geometry of the divider surface is characterized as:

$$H(\tilde{x}, \tilde{t}) = b(\tilde{x}) + \tilde{a} \sin \frac{2\pi}{\lambda}(\tilde{x} - C\tilde{t}), \tag{1}$$

where $b(\tilde{x}) = b_0 + \bar{K}\tilde{x}$. The relevant equations for the present flow model are given as:

$$\frac{\partial \tilde{u}}{\partial \tilde{x}} + \frac{\partial \tilde{v}}{\partial \tilde{y}} = 0, \tag{2}$$

$$\rho_f \left(\frac{\partial \tilde{u}}{\partial \tilde{t}} + \tilde{u} \frac{\partial \tilde{u}}{\partial \tilde{x}} + \tilde{v} \frac{\partial \tilde{u}}{\partial \tilde{y}} \right) = -\frac{\partial \tilde{p}}{\partial \tilde{x}} + \frac{\partial}{\partial \tilde{x}} S_{xx} + \frac{\partial}{\partial \tilde{y}} S_{xy} - \sigma B_0^2 \tilde{u} + g \left[(1-F) \rho_{f_0} \zeta (T - T_0) - (\rho_p - \rho_{f_0})(F - F_0) \right], \tag{3}$$

$$\rho_f \left(\frac{\partial \tilde{v}}{\partial \tilde{t}} + \tilde{v} \frac{\partial \tilde{u}}{\partial \tilde{x}} + \tilde{v} \frac{\partial \tilde{v}}{\partial \tilde{y}} \right) = -\frac{\partial \tilde{p}}{\partial \tilde{y}} + \frac{\partial}{\partial \tilde{x}} S_{yx} + \frac{\partial}{\partial \tilde{y}} S_{yy} + g \left[(1-F) \rho_{f_0} \zeta (T - T_0) - (\rho_p - \rho_{f_0})(F - F_0) \right] \tag{4}$$

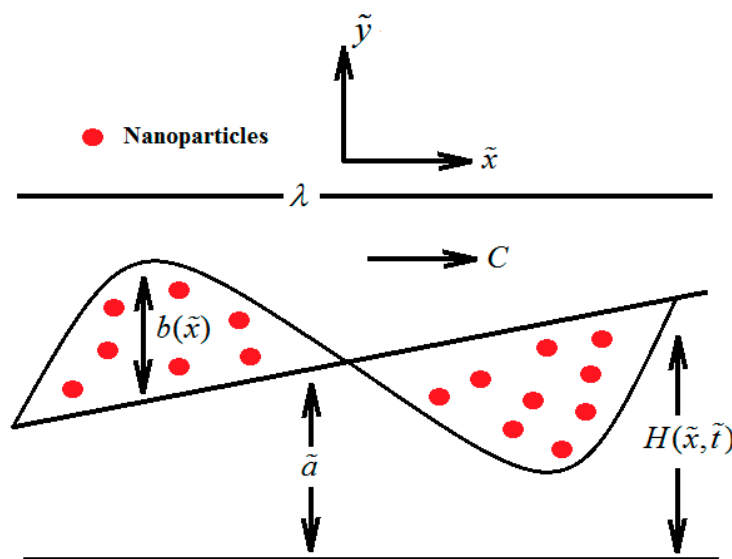


Figure 1. Geometry of the problem.

The concentration and energy equations are:

$$(\rho c)_f \left(\frac{\partial T}{\partial \tilde{t}} + \tilde{u} \frac{\partial T}{\partial \tilde{x}} + \tilde{v} \frac{\partial T}{\partial \tilde{y}} \right) = \kappa \left(\frac{\partial^2 T}{\partial \tilde{x}^2} + \frac{\partial^2 T}{\partial \tilde{y}^2} \right) + (\rho c)_p D_B \left(\frac{\partial T}{\partial \tilde{x}} \frac{\partial F}{\partial \tilde{x}} + \frac{\partial F}{\partial \tilde{y}} \frac{\partial T}{\partial \tilde{y}} \right) + \frac{D_T}{T_0} \left(\left(\frac{\partial T}{\partial \tilde{x}} \right)^2 + \left(\frac{\partial T}{\partial \tilde{y}} \right)^2 \right) - \frac{\partial q_r}{\partial \tilde{y}} + Q_0, \tag{5}$$

$$\left(\frac{\partial F}{\partial \tilde{t}} + \tilde{u} \frac{\partial F}{\partial \tilde{x}} + \tilde{v} \frac{\partial F}{\partial \tilde{y}} \right) = D_B \left(\frac{\partial^2 F}{\partial \tilde{x}^2} + \frac{\partial^2 F}{\partial \tilde{y}^2} \right) + \frac{D_T}{T_0} \left(\frac{\partial^2 T}{\partial \tilde{x}^2} + \frac{\partial^2 T}{\partial \tilde{y}^2} \right) - k_1 (F - F_0). \tag{6}$$

The radiative heat flux q_r under the approximation of Roseland for radiation is defined as:

$$q_r = -\frac{\partial T^4}{\partial \tilde{y}} \left[\frac{4\tilde{\sigma}}{3k} \right], \tag{7}$$

In the above equations, $\tilde{\sigma}$ is Stefan–Boltzmann constant and is mean retention steady. The temperature term can be stretched out (T^4) about a free stream temperature (T_0). Since the temperature inside the nanoparticles of blood flow is extremely small, it tends to be composed as:

$$T^4 = T_0^4 + 4T_0^3(T - T_0) + 6T_0^2(T - T_0)^2 + \dots \tag{8}$$

The above equation can be modified as:

$$T^4 \cong 4T_0^3(T - T_0), \tag{9}$$

Using Equation (9) into Equation (7) we get:

$$q_r = -\frac{16\bar{\sigma}}{3k} \frac{\partial T}{\partial y}. \tag{10}$$

For the non-Newtonian Jeffrey fluid, the extra stress tensor is defined as:

$$S = \frac{\mu}{1 + \lambda_1} (\dot{\gamma} + \lambda_2 \ddot{\gamma}), \tag{11}$$

Defining the non-dimensional quantities:

$$\begin{aligned} x &= \frac{\tilde{x}}{\lambda}, \quad y = \frac{\tilde{y}}{b_0}, \quad t = \frac{\tilde{t}}{\lambda}, \quad u = \frac{\tilde{u}}{c}, \quad v = \frac{\tilde{v}}{c\delta}, \quad p = \frac{\tilde{p}b_0^2}{\lambda\mu c}, \quad h = \frac{\tilde{h}}{b_0}, \quad \phi = \frac{\tilde{\phi}}{b_0}, \quad \text{Re} = \frac{\tilde{c}\rho\bar{a}}{\mu}, \quad \delta = \frac{b_0}{\lambda}, \\ \theta &= \frac{T-T_0}{T_1-T_0}, \quad \Phi = \frac{F-F_0}{F_1-F_0}, \quad Gr_F = \frac{gb_0^3(\rho_p-\rho_{f_0})(F_1-F_0)}{\rho_{f_0}v^2}, \quad M = \sqrt{\frac{B_0^2\bar{a}^2\sigma}{\mu_f}}, \quad N_b = \frac{(\rho c)_p D_B(F_1-F_0)}{\kappa}, \\ \gamma &= \frac{k_1 b_0^2}{v}, \quad N_t = \frac{(\rho c)_p D_T(T_1-T_0)}{\kappa T_0}, \quad Pr = \frac{v(\rho c)_f}{\kappa}, \quad Gr_T = \frac{\zeta gb_0^3(T_1-T_0)(1-F_0)}{\rho_{f_0}v^2}, \quad \beta = \frac{Q_0 b_0^2}{(T_1-T_0)v c_p}, \\ \gamma &= \frac{k_1 b_0^2}{v}, \quad R_d = \frac{16\bar{\sigma}T_0^3}{3k\mu c_f}, \quad S = \frac{b_0}{\mu c} S. \end{aligned} \tag{12}$$

Using Equation (12) into the governing equations and after dropping the tilde, the resulting equations are

$$\frac{1}{1 + \lambda_1} \frac{\partial^2 u}{\partial y^2} + -M^2 u + Gr_T \theta - Gr_F \Phi - \frac{\partial p}{\partial x} = 0, \tag{13}$$

$$\left(\frac{1}{Pr} + R_d\right) \frac{\partial^2 \theta}{\partial y^2} + N_b \frac{\partial \theta}{\partial y} \frac{\partial \Phi}{\partial y} + N_t \left(\frac{\partial \theta}{\partial y}\right)^2 + \beta = 0, \tag{14}$$

$$\frac{\partial^2 \Phi}{\partial y^2} + \frac{N_t}{N_b} \left(\frac{\partial^2 \theta}{\partial y^2}\right) - \gamma \Phi = 0, \tag{15}$$

Subject to the respective boundary conditions:

$$\begin{cases} \frac{\partial u(0)}{\partial y} = 0, \quad \theta(0) = 0, \quad \Phi(0) = 0, \\ u(h) = 0, \quad \theta(h) = 1, \quad \Phi(h) = 1, \end{cases} \tag{16}$$

where $h = 1 + \frac{\lambda \bar{K} x}{b_0} + \phi \sin 2\pi(x - t)$ and $\phi(0 \leq \phi \leq 1)$ the amplitude ratio.

3. Solution of the Problem

The homotopy perturbation method (HPM) is utilized to find the solution of the above non-linear coupled fractional differential equation. The homotopy for Equations (13)–(15) can be composed as:

$$\hbar(w, q) = (1 - q)(L_1(w) - L_1(\tilde{w}_0)) + q\left(L_1(w) - M^2 w - \frac{\partial p}{\partial x} + Gr_T \vartheta - Gr_F \Theta\right), \tag{17}$$

$$\hbar(\vartheta, q) = (1 - q)(L_2(\vartheta) - L_2(\tilde{\vartheta}_0)) + q\left(L_2(\vartheta) + \frac{Pr}{1 + R_d Pr} \left(N_b \frac{\partial \Theta}{\partial y} \frac{\partial \vartheta}{\partial y} + N_t \left(\frac{\partial \vartheta}{\partial y}\right)^2 + \beta\right)\right), \tag{18}$$

$$\hbar(\Theta, q) = (1 - q)(L_2(\Theta) - L_2(\tilde{\Theta}_0)) + q\left(L_2(\Theta) + \frac{N_f}{N_b} \frac{\partial^2 \vartheta}{\partial y^2} - \gamma\Theta\right), \tag{19}$$

The linear operators and initial guesses are defined as:

$$L_1 = \frac{1}{1 + \lambda_1} \frac{\partial^2}{\partial y^2} \tag{20}$$

$$L_2 = \frac{\partial^2}{\partial y^2} \tag{21}$$

and the initial guesses are:

$$\tilde{w}_0 = (1 + \lambda_1)(y^2 - h^2) \tag{22}$$

$$\tilde{\Theta}_0 = \tilde{\vartheta}_0 = \frac{y}{h} \tag{23}$$

Defining the following expansion:

$$\begin{aligned} w(x, y) &= w_0(x, y) + qw_1(x, y) + q^2w_2(x, y) + \dots, \\ \Theta(x, y) &= \Theta_0(x, y) + q\Theta_1(x, y) + q^2\Theta_2(x, y) + \dots, \\ \vartheta(x, y) &= \vartheta_0(x, y) + q\vartheta_1(x, y) + q^2\vartheta_2(x, y) + \dots, \end{aligned} \tag{24}$$

By applying the procedure of HPM, we obtained the solution as $q \rightarrow 1$. For this reason, utilizing Equation (24) in Equations (17)–(19) and looking at the forces of q , we get an arrangement of linear differential equation with their significant boundary conditions. The resulting solutions can be written in the following format:

$$\begin{aligned} u(x, y) &= w(x, y)|_{q \rightarrow 1} = w_0(x, y) + w_1(x, y) + w_2(x, y) + \dots, \\ \Phi(x, y) &= \Theta(x, y)|_{q \rightarrow 1} = \Theta_0(x, y) + \Theta_1(x, y) + \Theta_2(x, y) + \dots, \\ \theta(x, y) &= \vartheta(x, y)|_{q \rightarrow 1} = \vartheta_0(x, y) + \vartheta_1(x, y) + \vartheta_2(x, y) + \dots, \end{aligned} \tag{25}$$

The last arrangement of temperature profile, velocity profile and nanoparticle concentration profile are composed as:

$$u(x, y) = u_0 + u_1y^2 + u_2y^3 + u_3y^4 + u_4y^5 + u_5y^6, \tag{26}$$

$$\theta(x, y) = \theta_0 + \theta_1y^2 + \theta_2y^3 + \theta_3y^4, \tag{27}$$

$$\Phi(x, y) = \Phi_0 + \Phi_1y + \Phi_2y^2 + \Phi_3y^3 + \Phi_4y^4, \tag{28}$$

The constants $u_m, \theta_m, \Phi_m (m = 1, 2, 3 \dots)$ showing up in the above equations can be discover utilizing routine estimations.

The instantaneous volume rate is defined as

$$Q(t, x) = \int_0^h u dy. \tag{29}$$

The non-dimensional kind of pressure rise and friction power is at the wall with a length of the non-uniform channel L is given by:

$$\Delta P_L(t, x) = \int_0^{\frac{L}{\lambda}} \left(\frac{dp}{dx}\right) dx, \tag{30}$$

$$\Delta F_L(t, x) = \int_0^{\frac{L}{\lambda}} \left(\frac{dp}{dx}\right) dx \tag{31}$$

4. Results and Discussion

In this portion, the impact of nanofluid qualities on peristaltic blood flow design is contemplated graphically under the impacts of magnetohydrodynamics, thermal radiation and chemical reaction response in the framework of drug delivery. Correlation of numerical after effects of velocity profile additionally showed in Table 1 for Newtonian, non-Newtonian, nanofluid and non-nanofluid. A graphical response of the velocity profile, temperature profile and friction profile is exhibited in Figures 2–4 with recently distributed outcomes [26] by taking $R_d = \gamma = 0$ in Equations (17)–(19). It may be seen from these assumptions that our outcomes are in phenomenal concurrence with recently distributed outcomes which uncovers that present strategy and the present outcomes are right. Computational programming “Mathematica (10.3 v)” has been utilized to create all required numerical outlines. The integral results in Equations (30) and (31) are comprehended numerically with the assistance of the following parameters:

$$Q = \bar{Q} + \phi \sin 2\pi(x - t), \tag{32}$$

and

$$K = 5 \times 10^{-5}, \lambda = L = 10 \text{ cm}, b_0 = 1 \times 10^{-2} \text{ cm}. \tag{33}$$

Table 1. Numerical results of velocity field for Newtonian, non-Newtonian, nano and non-nanofluid.

	$u(x,y)$	$u(x,y)$	$u(x,y)$	$u(x,y)$
	$\lambda_1 = 0$	$\lambda_1 \neq 0$	$\lambda_1 = 0$	$\lambda_1 \neq 0$
h	$Gr_F = 0, Gr_T = 0$	$Gr_F = 0, Gr_T = 0$	$Gr_F \neq 0, Gr_T \neq 0$	$Gr_F \neq 0, Gr_T \neq 0$
0	0.6467	0.6458	0.6431	0.6456
0.115	0.6405	0.6397	0.6370	0.6395
0.230	0.6219	0.6212	0.6184	0.6211
0.345	0.5907	0.5903	0.5874	0.5903
0.460	0.5469	0.5467	0.5438	0.5468
0.575	0.4901	0.4903	0.4874	0.4904
0.690	0.4201	0.4206	0.4178	0.4207
0.805	0.3365	0.3372	0.3347	0.3373
0.920	0.2390	0.2397	0.2376	0.2398
1.035	0.1270	0.1275	0.1263	0.1275
1.115	0	0	0	0

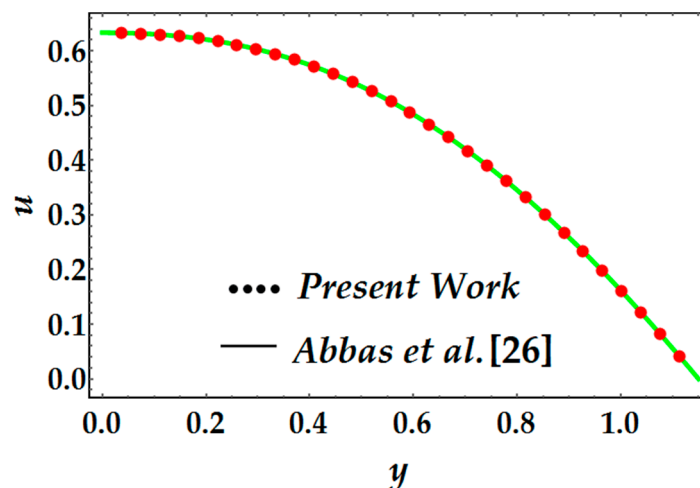


Figure 2. Comparison of velocity profile.

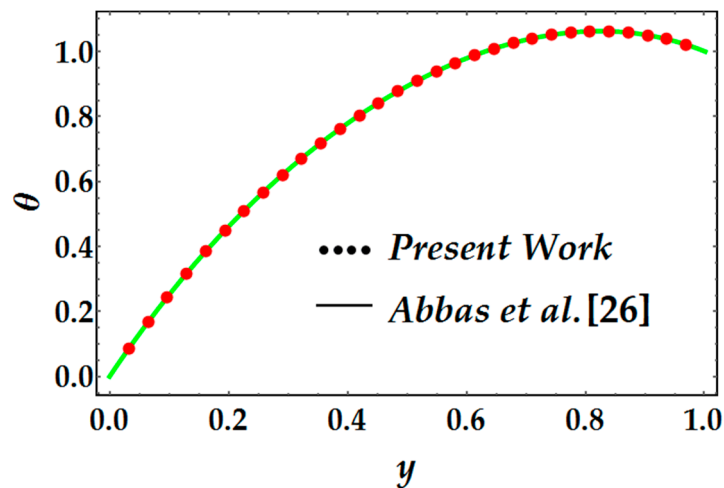


Figure 3. Comparison of temperature profile.

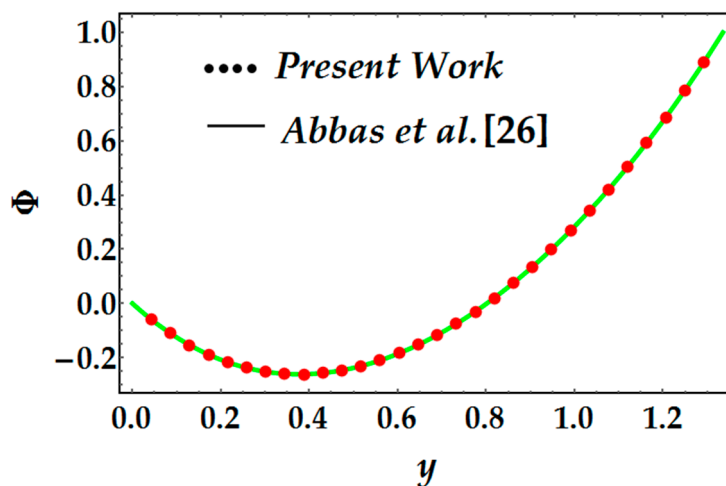


Figure 4. Comparison of concentration profile.

Figures 5–7 show temperature profile for heat source/sink parameter β , Brownian movement parameter, Prandtl number, radiation parameter, and thermophoresis parameter. It tends to be seen from Figure 5 that an upgrade in the radiation parameter will give a noteworthy opposition in the temperature profile. At the point when the radiation parameter builds, it improves the movement of electromagnetic waves while heat conduction ends up being smothered. Since dispersion heat exchange happens because of an irregular proliferation of atoms, when it is extinguished, then the neighboring particles spread less, and the vitality exchange rate turns out to be less productive between one another. In addition, the time size of diffusive heat exchange is larger than the radiative heat exchange. Furthermore, it is likewise seen in Figure 5 that an augmentation in heat source/sink parameter altogether upgrades the temperature profile. Before we talk about the graphical outcomes, it is fundamental to compose the significance of Brownian motion and thermophoresis parameters. Brownian motion of nanofluid particles was proposed because small particles in general move all the more unequivocally and could be beneficial to heat transport. The molecule in nanofluid experience unpredictable development and the irregular impacts of the encompassing fluid particles happened. This movement is called Brownian motion. The implications of a Brownian motion-incited molecule were relied upon to expand the heat transport among particles and in this way increment heat radiation of the nanofluids. It is very well may be seen from Figure 6 for higher estimations of the Brownian motion parameter, temperature profile extraordinarily increments and comparative behavior has been watched for higher estimates of the thermophoresis parameter. Physically, when the thermophoresis

parameter upgrades, thermophoretic power occurs because of blends of versatile particles, the results of which will improve the temperature profile. Figure 7 is set up to see the behavior of the Prandtl number on temperature profile. We can see from this assumption that when the Prandtl number builds, then the temperature profile rises. Physically, when the Prandtl number is minimal then it concludes that heat diffusivity is additionally overwhelming while expansive estimations of Prandtl number reveals that momentum is progressive. In different heat exchange cases, the Prandtl number is entirely positive to control the force and thermal boundary layer thickness.

Figures 8 and 9 demonstrates the behavior of concentration profile against chemical reaction parameter γ , Brownian motion parameter, radiation parameter thermophoresis parameter. It is found from Figure 8 that with the expansion in chemical reaction response parameter γ , the concentration profile diminishes. Yet from the central point, its behavior ends up inverse and begins to increment. In addition, it is additionally discovered that the radiation parameter likewise enhances the concentration profile (see Figure 8). Figure 9 is dedicated to viewing the impact of N_b and N_t on concentration profile. In the two cases, the concentration profile has an inverse response as expanding in N_b and N_t .

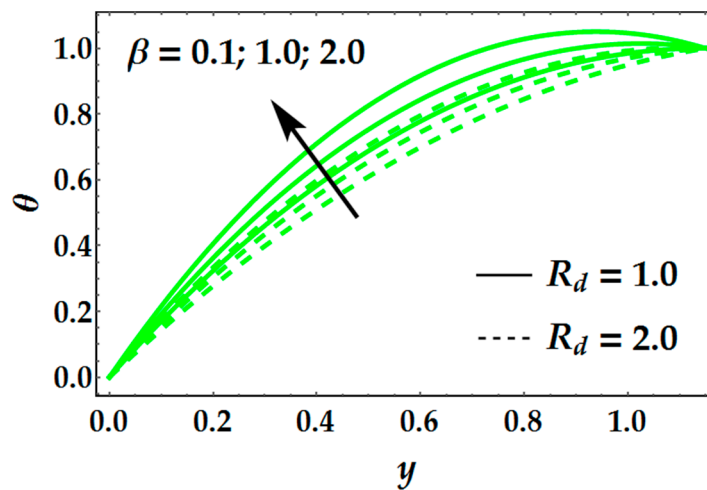


Figure 5. Temperature profile for multiple values of β and R_d .

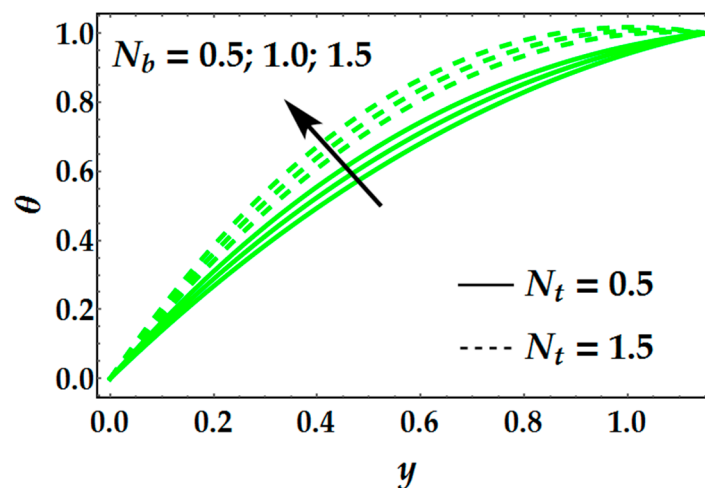


Figure 6. Temperature profile for multiple values of N_b and N_t .

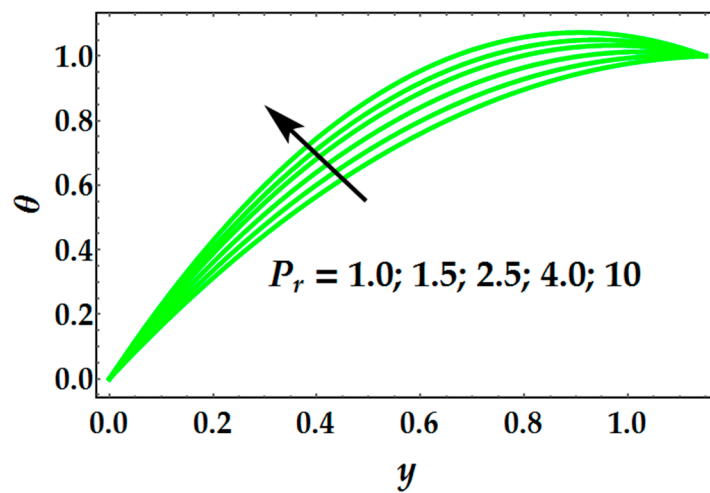


Figure 7. Temperature profile for multiple values of P_r .

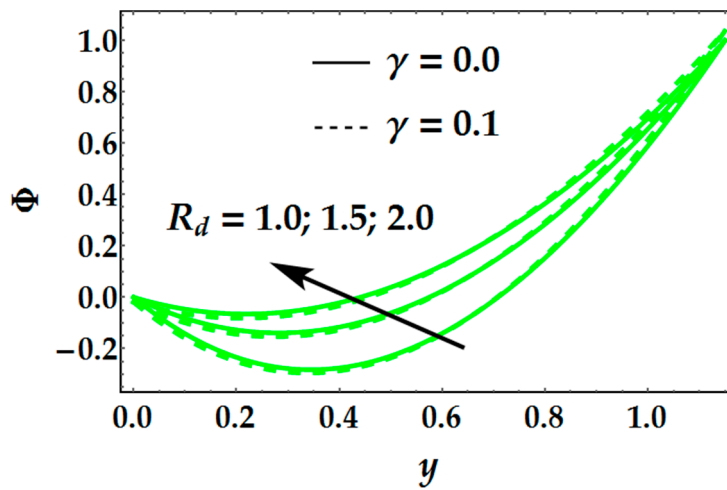


Figure 8. Concentration profile for multiple values of γ and R_d .

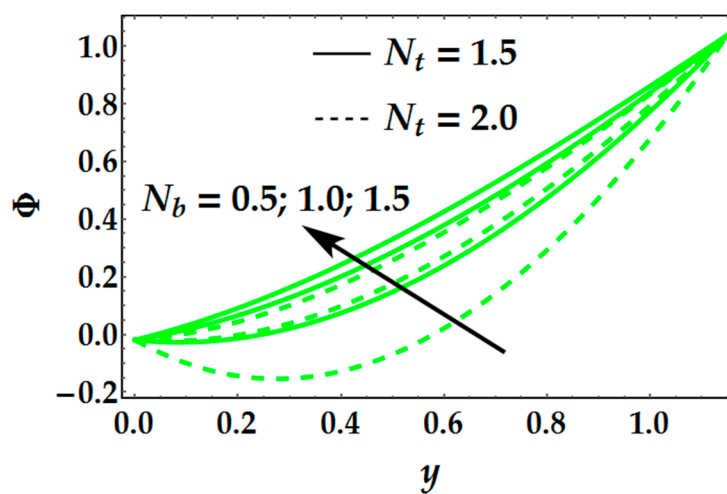


Figure 9. Concentration profile for multiple values of N_b and N_t .

Figures 10 and 11 show the variety of friction powers against various estimations of density Grashof number Gr_F , thermal Grashof number Gr_T , Hartmann number M and fluid parameter λ_1 . It is evident from Figure 10 that when the basic density Grashof number builds, then it gives colossal

support to upgrade the friction force while its behavior at the origin of higher estimations of thermal Grashof number. Figure 11 shows that an upgrade in Hartmann number M will continue to ascent the friction force while when the liquid is non-Newtonian $\lambda_1 \neq 0$, then it makes checked protection from friction forces. Figures 12 and 13 demonstrate the characteristics of pumping against various included parameters, for instance, Hartmann number M , basic density Grashof number Gr_F and thermal Grashof number Gr_T . It is additionally an engaging component of peristalsis and especially supportive in transporting different sorts of natural fluids in the human body. It can be seen from Figure 12 that because of higher estimations of a magnetic field, the pumping rate diminishes, and the pumping rate indicates comparative behavior against basic density Grashof number (see Figure 13). It is seen from Figure 13 that pumping rate increases overall for higher estimations of thermal Grashof number. Figures 14 and 15 portrays the behavior of pressure rise versus time against various values of basic density Grashof number, thermal Grashof number, Hartmann number, and fluid parameter. It is found here that pressure rise demonstrates opposite behavior when contrasted with friction forces.

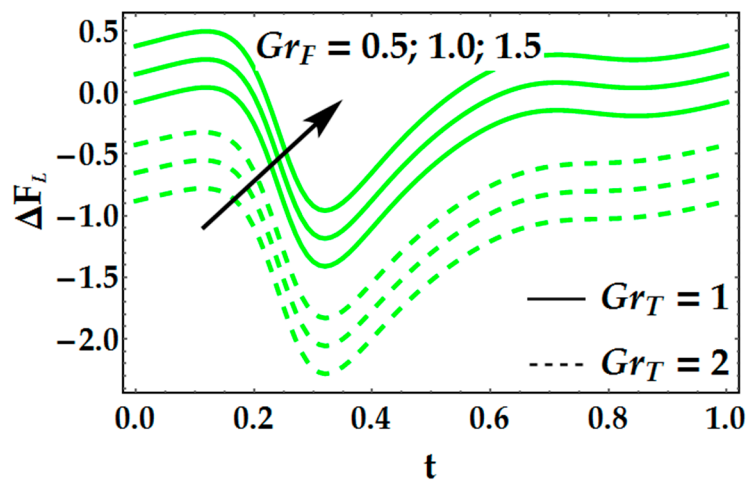


Figure 10. Friction force for multiple values of Gr_T and Gr_F .

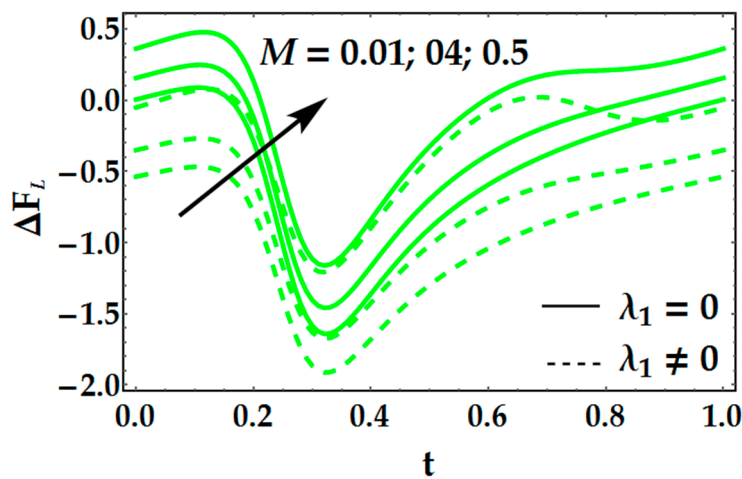


Figure 11. Friction forces for multiple values of M and λ_1 .

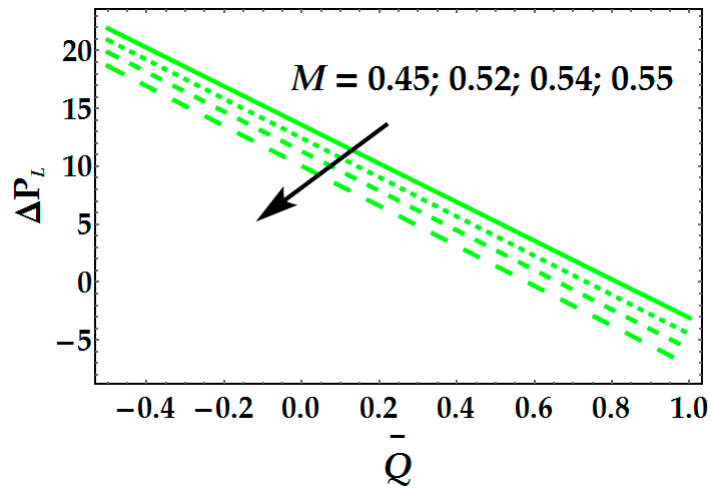


Figure 12. Pressure rise vs. average volume flow rate for multiple values of M .

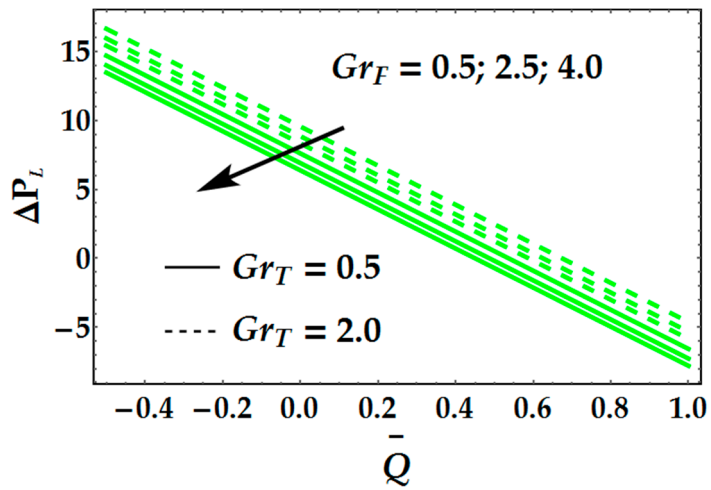


Figure 13. Pressure rise vs. average volume flow rate for multiple values of Gr_T and Gr_F .

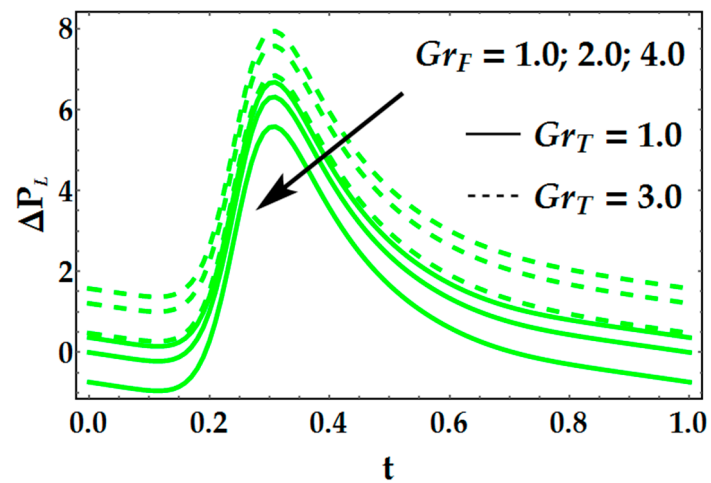


Figure 14. Pressure rise vs. time for multiple values of Gr_T and Gr_F .

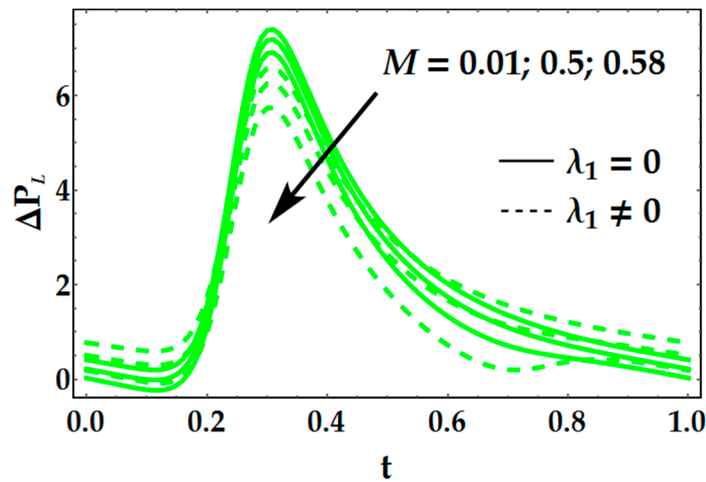


Figure 15. Pressure rise vs. time for multiple values of M and λ_1 .

To see the behavior of a velocity profile, Figures 16 and 17 are portrayed. Figure 16 reveals the behavior of basic density Grashof number and thermal Grashof number. It is seen in this figure that the higher effect of Gr_F shows inverse behavior close to the wall of the channel. At the point when $y > 0.5$ the speed of velocity reduces because of the augmentation in basic density Grashof number while it shows a different response for $y < 0.5$. Additionally, it is seen that the thermal Grashof number shows direct inverse behavior when contrasted with the basic density Grashof number. It is seen in Figure 17 that Hartmann number M neglects to give a noteworthy obstruction close to the wall at $y > 0.6$. However, it will produce a remarkable opposition in the center point of the channel, since when the magnetic field is connected, a resistive power (known as the “Lorentz force”) happens that restricts the stream and will diminish the speed when $y < 0.6$. Further, it is discovered that the greatness of the speed decrease when the fluid is non-Newtonian in the locale ($\lambda_1 \neq 0$) in the region $y < 0.6$, while its behavior is inverse for $y > 0.6$ (see Figure 17).

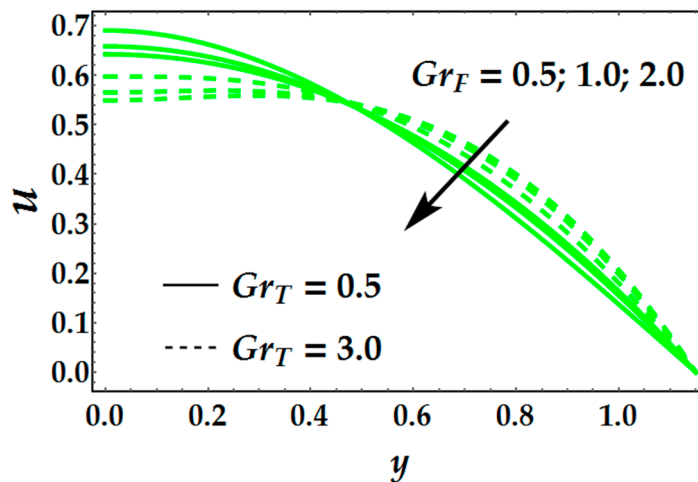


Figure 16. Velocity profile for multiple values of Gr_T and Gr_F .

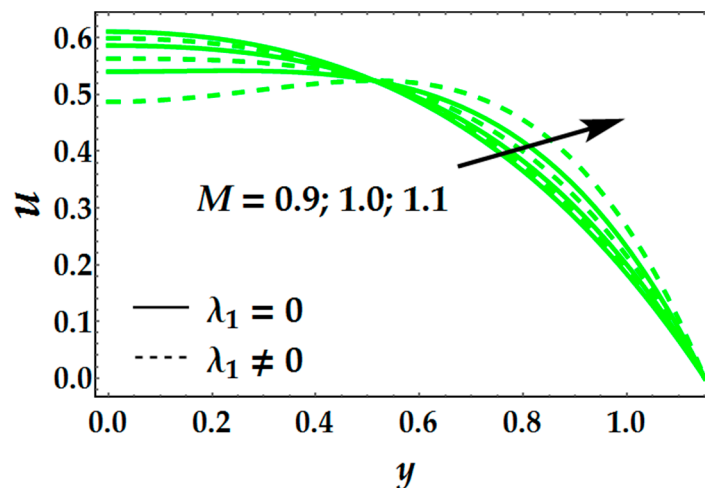


Figure 17. Velocity profile for multiple values of M and λ_1 .

5. Conclusions

The impact of nanofluid particles on the peristaltic bloodstream has been explored scientifically under the effects of thermal radiation and chemical response with the guide of the computational program Mathematica. The base liquid is considered as a Jeffrey fluid model within sight of an applied magnetic field. The administering flow is displayed for low Reynolds number and long wavelength. The diminished conditions are coupled to ordinary differential equations and, along with these equations, we have utilized the homotopy irritation strategy to acquire the series solution. To get the aftereffects of pressure rise, and friction force, numerical incorporation has been used. The resulting mathematical calculations have shown the following outcomes:

- Temperature profile increments with the augmentation in N_b , N_t , P_r and β parameters.
- Radiation parameter provides a significant resistance in temperature profile.
- Concentration profile increments, when Brownian movement parameter N_b increments while its behavior is inverse for higher estimations of thermophoresis parameter N_t .
- Chemical reaction parameter has an inverse behavior on concentration profile close to the wall.
- Radiation parameter also enhances significantly the concentration profile.
- Velocity profile shows converse behavior for higher values of thermal Grashof number and basic density Grashof number.
- Pumping rate increases for higher values of Hartmann number and thermal Grashof number.
- The present results reduce to Newtonian fluid model by taking $\lambda_1 = 0$ in the modeled equations.
- The present results are also compared with previously published results [26] by taking $R_d = \gamma = 0$ to validate the current results and methodology.

Author Contributions: Conceptualization and methodology, M.M.B.; writing—Review and editing, M.A.A.; Investigation, M.S.

Funding: This research received no external funding.

Conflicts of Interest: The authors declare no conflict of interest.

Nomenclature

\tilde{u}, \tilde{v}	velocity components
\tilde{x}, \tilde{y}	Cartesian coordinate
\tilde{p}	pressure in fixed frame
\tilde{a}	wave amplitude
$b(\tilde{x})$	width of the channel
\tilde{c}	wave velocity
Pr	Prandtl number
Re	Reynolds number
\tilde{t}	time
Gr_F	basic density Grashof number
Gr_T	thermal Grashof number
N_b	Brownian motion parameter
N_t	thermophoresis parameter
$\bar{K}(\ll 1)$	constant
B_0	magnetic field
We	Weissenberg number
Q	volume flow rate
T, F	temperature and concentration
g	acceleration due to gravity
D_B	Brownian diffusion coefficient
D_T	thermophoretic diffusion coefficient
K	mean absorption constant
M	Hartman number
\mathbf{S}	stress tensor
\tilde{k}	porosity parameter

Greek Symbols

γ	chemical reaction parameter
κ	nanofluid thermal conductivity
β	heat source/sink parameter
μ	viscosity of the fluid
Φ	nano- particle volume fraction
σ	electrical conductivity
δ	wave number
$\bar{\sigma}$	Stefan–Boltzmann constant
c_p	effective heat capacity of nanoparticle
ν	nanofluid kinematic viscosity
$(\rho)_p$	nanoparticle mass density
ρ_f	fluid density
ρ_{f_0}	fluid density at the reference temperature
ζ	volumetric expansion coefficient
$(\rho c)_f$	heat capacity of fluid
λ	wavelength (m)
ϕ	Amplitude ratio

References

1. Sun, C.; Lee, J.S.H.; Zhang, M. Magnetic nanoparticles in MR imaging and drug delivery. *Adv. Drug Deliv. Rev.* **2018**, *60*, 1252–1265. [[CrossRef](#)] [[PubMed](#)]
2. Berry, C.C. Progress in functionalization of magnetic nanoparticles for applications in biomedicine. *J. Phys. D Appl. Phys.* **2009**, *42*, 224003. [[CrossRef](#)]
3. McBain, S.C.; Yiu, H.H.; Dobson, J. Magnetic nanoparticles for gene and drug delivery. *Int. J. Nanomed.* **2008**, *3*, 169.

4. Cho, K.; Wang, X.U.; Nie, S.; Shin, D.M. Therapeutic nanoparticles for drug delivery in cancer. *Clin. Cancer Res.* **2008**, *14*, 1310–1316. [[CrossRef](#)] [[PubMed](#)]
5. Veisoh, O.; Gunn, J.W.; Zhang, M. Design and fabrication of magnetic nanoparticles for targeted drug delivery and imaging. *Adv. Drug Deliv. Rev.* **2010**, *62*, 284–304. [[CrossRef](#)]
6. Solanki, A.; Kin, J.D.; Lee, K.B. *Nanotechnology for Regenerative Medicine: Nanomaterials for Stem Cell Imaging; Future Medicine*: London, UK, 2008; Volume 3, pp. 567–578.
7. Misra, J.C.; Sinha, A.; Shit, G.C. Theoretical analysis of blood flow through an arterial segment having multiple stenoses. *J. Mech. Med. Biol.* **2008**, *8*, 265–279. [[CrossRef](#)]
8. Akbar, N.S.; Nadeem, S.; Hayat, T.; Hendi, A.A. Peristaltic flow of a nanofluid with slip effects. *Meccanica* **2012**, *47*, 1283–1294. [[CrossRef](#)]
9. Tripathi, D.; Bég, O.A. A study on peristaltic flow of nanofluids: Application in drug delivery systems. *Int. J. Heat Mass Transf.* **2014**, *70*, 61–70. [[CrossRef](#)]
10. Sheikholeslami, M.; Abelman, S. Two-phase simulation of nanofluid flow and heat transfer in an annulus in the presence of an axial magnetic field. *IEEE Trans. Nanotechnol.* **2015**, *14*, 561–569. [[CrossRef](#)]
11. Akbar, N.S.; Raza, M.; Ellahi, R. Influence of induced magnetic field and heat flux with the suspension of carbon nanotubes for the peristaltic flow in a permeable channel. *J. Magn. Magn. Mater.* **2015**, *381*, 405–415. [[CrossRef](#)]
12. Rashidi, M.; Bhatti, M.; Abbas, M.; Ali, M. Entropy generation on MHD blood flow of nanofluid due to peristaltic waves. *Entropy* **2016**, *18*, 117. [[CrossRef](#)]
13. Bhatti, M.M.; Zeeshan, A.; Ellahi, R. Simultaneous effects of coagulation and variable magnetic field on peristaltically induced motion of Jeffrey nanofluid containing gyrotactic microorganism. *Microvasc. Res.* **2017**, *110*, 32–42. [[CrossRef](#)] [[PubMed](#)]
14. Iftikhar, N.; Rehman, A.; Sadaf, H.; Khan, M.N. Impact of wall properties on the peristaltic flow of Cu-water nano fluid in a non-uniform inclined tube. *Int. J. Heat Mass Transf.* **2018**, *125*, 772–779. [[CrossRef](#)]
15. Abdelsalam, S.I.; Bhatti, M.M. The study of non-Newtonian nanofluid with hall and ion slip effects on peristaltically induced motion in a non-uniform channel. *RSC Adv.* **2018**, *8*, 7904–7915. [[CrossRef](#)]
16. Mekheimer, K.S.; Hasona, W.M.; Abo-Elkhair, R.E.; Zaher, A.Z. Peristaltic blood flow with gold nanoparticles as a third grade nanofluid in catheter: Application of cancer therapy. *Phys. Lett. A* **2018**, *382*, 85–93. [[CrossRef](#)]
17. Akram, S.; Zafar, M.; Nadeem, S. Peristaltic transport of a Jeffrey fluid with double-diffusive convection in nanofluids in the presence of inclined magnetic field. *Int. J. Geometr. Methods Mod. Phys.* **2018**, *15*, 1850181. [[CrossRef](#)]
18. Prakash, J.; Siva, E.P.; Tripathi, D.; Kuharat, S.; Bég, O.A. Peristaltic pumping of magnetic nanofluids with thermal radiation and temperature-dependent viscosity effects: Modelling a solar magneto-biomimetic nanopump. *Renew. Energy* **2019**, *133*, 1308–1326. [[CrossRef](#)]
19. Abdelsalam, S.I.; Bhatti, M.M. New Insight into AuNP Applications in Tumour Treatment and Cosmetics through Wavy Annuli at the Nanoscale. *Sci. Rep.* **2019**, *9*, 260. [[CrossRef](#)]
20. Ray, A.K.; Vasu, B.; Bég, O.A.; Gorla, R.S.; Murthy, P.V. Homotopy Semi-Numerical Modeling of Non-Newtonian Nanofluid Transport External to Multiple Geometries Using a Revised Buongiorno Model. *Inventions* **2019**, *4*, 54. [[CrossRef](#)]
21. Abbas, M.A.; Hussain, I. Statistical Analysis of the Mathematical Model of Entropy Generation of Magnetized Nanofluid. *Inventions* **2019**, *4*, 32. [[CrossRef](#)]
22. Waqas, H.; Khan, S.U.; Imran, M.; Bhatti, M.M. Thermally developed Falkner-Skan bioconvection flow of a magnetized nanofluid in the presence of motile gyrotactic microorganism: Buongiorno's nanofluid model. *Phys. Scr.* **2019**, *94*, 115304. [[CrossRef](#)]
23. Tlili, I.; Bhatti, M.M.; Hamad, S.M.; Barzinjy, A.A.; Sheikholeslami, M.; Shafee, A. Macroscopic modeling for convection of Hybrid nanofluid with magnetic effects. *Phys. A Stat. Mech. Appl.* **2019**, *534*, 122136. [[CrossRef](#)]
24. Abdelsalam, S.; Bhatti, M.M.; Zeeshan, A.; Riaz, A.; Beg, O.A. Metachronal propulsion of a magnetized particle-fluid suspension in a ciliated channel with heat and mass transfer. *Phys. Scr.* **2019**, *94*, 115301. [[CrossRef](#)]

25. Waqas, H.; Khan, S.U.; Hassan, M.; Bhatti, M.M.; Imran, M. Analysis on the bioconvection flow of modified second-grade nanofluid containing gyrotactic microorganisms and nanoparticles. *J. Mol. Liq.* **2019**, *291*, 111231. [[CrossRef](#)]
26. Abbas, M.A.; Bai, Y.Q.; Rashidi, M.M.; Bhatti, M.M. Application of drug delivery in magnetohydrodynamics peristaltic blood flow of nanofluid in a non-uniform channel. *J. Mech. Med. Biol.* **2016**, *16*, 1650052. [[CrossRef](#)]
27. Wang, F.; Shuai, Y.; Wang, Z.; Leng, Y.; Tan, H. Thermal and chemical reaction performance analyses of steam methane reforming in porous media solar thermochemical reactor. *Int. J. Hydrog. Energy* **2014**, *39*, 718–730. [[CrossRef](#)]
28. Akbarzadeh, P. The onset of MHD nanofluid convection between a porous layer in the presence of purely internal heat source and chemical reaction. *J. Therm. Anal. Calorim.* **2018**, *131*, 2657–2672. [[CrossRef](#)]
29. Yadav, D. The onset of longitudinal convective rolls in a porous medium saturated by a nanofluid with non-uniform internal heating and chemical reaction. *J. Therm. Anal. Calorim.* **2019**, *135*, 1107–1117. [[CrossRef](#)]
30. Chen, X.; Wang, F.; Han, Y.; Yu, R.; Cheng, Z. Thermochemical storage analysis of the dry reforming of methane in foam solar reactor. *Energy Convers. Manag.* **2018**, *158*, 489–498. [[CrossRef](#)]
31. Chen, X.; Wang, F.; Yan, X.; Han, Y.; Cheng, Z.; Jie, Z. Thermochemical performance of solar driven CO₂ reforming of methane in volumetric reactor with gradual foam structure. *Energy* **2018**, *151*, 545–555. [[CrossRef](#)]



© 2019 by the authors. Licensee MDPI, Basel, Switzerland. This article is an open access article distributed under the terms and conditions of the Creative Commons Attribution (CC BY) license (<http://creativecommons.org/licenses/by/4.0/>).